

# Journal of Materials Chemistry A

Accepted Manuscript



This is an *Accepted Manuscript*, which has been through the Royal Society of Chemistry peer review process and has been accepted for publication.

*Accepted Manuscripts* are published online shortly after acceptance, before technical editing, formatting and proof reading. Using this free service, authors can make their results available to the community, in citable form, before we publish the edited article. We will replace this *Accepted Manuscript* with the edited and formatted *Advance Article* as soon as it is available.

You can find more information about *Accepted Manuscripts* in the [Information for Authors](#).

Please note that technical editing may introduce minor changes to the text and/or graphics, which may alter content. The journal's standard [Terms & Conditions](#) and the [Ethical guidelines](#) still apply. In no event shall the Royal Society of Chemistry be held responsible for any errors or omissions in this *Accepted Manuscript* or any consequences arising from the use of any information it contains.

# Growth-Controlled NiCo<sub>2</sub>S<sub>4</sub> Nanosheet Arrays with Self-Decorated Nanoneedles for High-Performance Pseudocapacitors

Liyang Lin<sup>a,b†</sup>, Jianlin Liu<sup>a,c†</sup>, Tianmo Liu<sup>b\*</sup>, Jinghua Hao<sup>a,b</sup>, Kemeng Ji<sup>a</sup>, Rong Sun<sup>a</sup>,  
Wen Zeng<sup>b</sup>, Zhongchang Wang<sup>a\*</sup>

<sup>a</sup>*Advanced Institute for Materials Research, Tohoku University, 2-1-1 Katahira, Aoba-ku, Sendai 980-8577, Japan*

<sup>b</sup>*College of Materials Science and Engineering, Chongqing University, Chongqing 400030, China*

<sup>c</sup>*Department of Applied Physics, Chongqing University, Chongqing 400044, China*

**ABSTRACT:** We report a synthesis of NiCo<sub>2</sub>S<sub>4</sub> nanosheet arrays with self-decorated nanoneedles on nickel foams by a facile and efficient two-step hydrothermal approach. We demonstrate that morphologies of various three-dimensional nanostructures such as nanoneedles arrays, nanosheet arrays, and nanoneedles-decorated nanosheet arrays can be manipulated by tuning the amount of the additive ammonium fluoride alone in the reaction. The unusual nanostructure of nanoneedles grown on surface of NiCo<sub>2</sub>S<sub>4</sub> nanosheet arrays shows a large electroactive surface area and superior electrochemical properties. The electrode made of the NiCo<sub>2</sub>S<sub>4</sub> nanosheet arrays with self-decorated nanoneedles shows greatly improved electrochemical performances with an ultrahigh specific capacitance of 2617.6 Fg<sup>-1</sup> at a current density of 15 mAcm<sup>-2</sup> and of 2051.0 Fg<sup>-1</sup> even at a current density of 30 mAcm<sup>-2</sup>. The electrode also exhibits an excellent cycling stability by retaining 93.2% of its original state after 5000 cycles, rendering the NiCo<sub>2</sub>S<sub>4</sub> nanosheet arrays with self-decorated nanoneedles a potential electrode material for high-performance supercapacitors.

## 1 Introduction

With the fast-growing need for energy and power, much effort has been devoted to the development of low-cost, high-storage and long-lifetime energy storage devices and energy conversion/storage systems.<sup>1-5</sup> Of the current protocols, supercapacitors have attracted a great deal of attentions due to their high power density, short charging time, and long cycle life.<sup>6-8</sup> For example, the reversible faradaic redox reactions take place at the electrode surface of pseudocapacitors, giving rise to a remarkably high specific capacitance.<sup>9</sup> Initially, RuO<sub>2</sub> has been demonstrated to be a pseudocapacitive material that exhibits good electrochemical performances,<sup>10</sup> but its high cost and toxic nature limit its wide application. To overcome these problems, transition metal oxides such as MnO<sub>2</sub><sup>11</sup>, NiO<sup>12</sup>, Co<sub>3</sub>O<sub>4</sub><sup>13</sup>, and NiCo<sub>2</sub>O<sub>4</sub><sup>14-16</sup> have been investigated intensively because they are environmentally friendly, controllable, and structurally stable. Most of them, however, show a low electric conductivity, which imposes a negative impact on electron transfer and ion exchange during the energy conversion process.

One typical example is NiCo<sub>2</sub>O<sub>4</sub>, which shows flexible morphologies and a high electrochemical activity,<sup>17-19</sup> yet a poor electric conductivity which cannot satisfy the requirement of fast electron transfer devices. One way to overcome this weakness is through vulcanizing NiCo<sub>2</sub>O<sub>4</sub> to NiCo<sub>2</sub>S<sub>4</sub>, which could increase conductivity by two orders of magnitude.<sup>20</sup> In particular, three-dimensional (3D) nanostructure arrays of NiCo<sub>2</sub>S<sub>4</sub>, which are grown on conducting substrates such as the Ni foam,<sup>21-23</sup> carbon fiber,<sup>25,26</sup> and carbon foam<sup>27</sup>, have been investigated. Such 3D nanostructures on Ni foam can be directly used as electrodes, thereby avoiding the “dead volume” caused by polymer binder. Moreover, the 3D nanostructures, e.g. nanosheets or nanoneedles, could also offer a large specific surface area and fast electron and ion transfer, thereby rendering it indispensable to design and fabricate these 3D nanostructures through a simple and convenient method.

Herein, we report direct growth of NiCo<sub>2</sub>S<sub>4</sub> nanosheet arrays with self-decorated nanoneedles on Ni foam by two-step solution reaction and demonstrate that in one-pot synthesis, nanoneedles are grown epitaxially on nanosheet arrays and can be tuned to appear or disappear by controlling the amount of NH<sub>4</sub>F additive alone under the same

reaction condition.<sup>28</sup> The electrochemical tests manifest that the electrode made of the prepared NiCo<sub>2</sub>S<sub>4</sub> nanosheet arrays with self-decorated nanoneedles (NiCo<sub>2</sub>S<sub>4</sub>-NSNs) possesses an ultrahigh specific capacitance of 2617.6 Fg<sup>-1</sup> at a current density of 15 mAcm<sup>-2</sup> and a barely declining capacitance even after 5000 cycles.

## 2 Experimental

### 2.1 Materials Preparation and Characterization

All chemicals were of analytical grade and used without further purification. The Ni foam was first immersed in 3 M HCl solution under ultrasonic cleaning for 20 min to remove the dirty and possible surface oxide layers. The treated Ni foam was then rinsed thoroughly with water and ethanol. To fabricate NiCo<sub>2</sub>O<sub>4</sub>-NSNs, 1 mmol nickel nitrate hexahydrate, 2 mmol cobalt nitrate hexahydrate, 6 mmol ammonium fluoride, and 15 mmol urea were dissolved in 50 mL deionized water under magnetic stirring for 30 min. The transparent solution was subsequently transferred into a 100 mL Teflon-lined stainless steel autoclave. A piece of treated Ni foam (2 cm × 3 cm) was immersed in the solution before sealing the autoclave. The autoclave was put into a muffle furnace and heated at 105°C for 4 h. The purple precursors on the Ni foam were washed ultrasonically several times with deionized water and ethanol. Lastly, the NiCo<sub>2</sub>O<sub>4</sub>-NSNs sample (named S<sub>0</sub>) was obtained after annealing at 350°C for 2 h. For comparison, we also synthesized a series of samples under identical reaction condition but with different hydrothermal treating time and ammonium fluoride concentration: 1 h and 6 mmol ammonium fluoride (S<sub>1</sub>), 2 h and 6 mmol (S<sub>2</sub>), 3 h and 6 mmol (S<sub>3</sub>), 4 h and 0 mmol (S<sub>4</sub>), and 4 h and 9 mmol (S<sub>5</sub>). To prepare NiCo<sub>2</sub>S<sub>4</sub>, the samples S<sub>0</sub> to S<sub>5</sub> were further immersed in 25 mM sodium sulfide hydrate solution, which were heated at 140°C for 9 h. After cooling down to room temperature, the as-obtained NiCo<sub>2</sub>S<sub>4</sub> samples (SS<sub>0</sub>, SS<sub>1</sub>, SS<sub>2</sub>, SS<sub>3</sub>, SS<sub>4</sub>, and SS<sub>5</sub>) were washed and dried at 60°C for 12 h.

Morphologies and microstructures were characterized with a JSM-7800F (JEOL) Field-Emission Scanning Electron Microscope (FE-SEM) and a JEM-2010F (JEOL) Transmission Electron Microscope (TEM)<sup>29-31</sup>. The composition and phase of the samples were evaluated by the X-ray diffraction (XRD). A Rigaku SmartLab 9MTP

diffraction with Cu  $K\alpha$  radiation operated at 40 kV and 200 mA was applied. The scanning rate was set to 0.01 deg.s<sup>-1</sup>.

## 2.2 Electrochemical measurements

The electrodes made of the SS<sub>0</sub>, SS<sub>5</sub>, S<sub>0</sub> samples with the Ni foam were used as working electrodes and saturated calomel electrodes, and Pt foil was used as reference and counter electrodes. Cyclic voltammetry (CV) and galvanostatic charge-discharge measurements were conducted in 2.0 M KOH solution by an electrochemical working station (Ivium Technology). The specific capacitance ( $C$ ) was calculated by using  $C = Idt/mdU$  or  $C = Idt/SdU$  in the discharge measurements, where  $I$  was discharge current density,  $U$  was the potential window,  $S$  was the electrode area, and  $t$  was the working time.<sup>14,22</sup> The electrochemical impedance spectra were collected using a frequency ranging from 100 kHz to 0.1 Hz. The nominal region of the electrodes SS<sub>0</sub>, SS<sub>5</sub>, and S<sub>0</sub> immersed in the electrolyte was controlled to be  $\sim 1 \times 0.5$  cm<sup>2</sup>. The average mass loading of SS<sub>0</sub>, SS<sub>5</sub>, and S<sub>0</sub> electrodes was 3.42, 3.24, and 3.3 mgcm<sup>-2</sup>, respectively.

## 2.3 Fabrication of flexible all-solid-state supercapacitors

The poly(vinyl alcohol)-LiCl (PVA-LiCl) polymer electrolyte was prepared by a typical process. 6 g PVA and 6 g LiCl were dissolved in 60 mL deionized water under stirring at 90 °C until the solution became clear. The all-solid-state supercapacitor was prepared by assembling PVA-LiCl gel electrolyte with two pieces of SS<sub>0</sub> electrodes ( $1 \times 1$  cm<sup>2</sup>) in a face-to-face way. The solid-state symmetric supercapacitor was obtained when the electrolyte was solidified at room temperature. The electrochemical tests of symmetric capacitors were performed in a two-electrode cell. The effective region of symmetric electrodes was controlled to be  $\sim 1 \times 0.5$  cm<sup>2</sup>. The average mass loading of the SS<sub>0</sub> electrodes was  $\sim 2.81$  mgcm<sup>-2</sup>.

# 3 Results and discussion

## 3.1 Synthesis and characterization

Figure 1 shows X-ray diffraction (XRD) patterns of the samples SS<sub>0</sub> and SS<sub>5</sub>,

and the sample  $S_0$  on Ni foam, where the peaks of Ni foam are highlighted by circles. In Fig. 1a and 1b, one can see five diffraction peaks at  $26.8^\circ$ ,  $31.6^\circ$ ,  $38.3^\circ$ ,  $50.5^\circ$ , and  $55.3^\circ$ , which correspond to (220), (311), (400), (511), and (440) planes of the cubic phase of  $NiCo_2S_4$  (20-0782), respectively. In Fig. 1c, there emerge five diffraction peaks at  $31.1^\circ$ ,  $36.7^\circ$ ,  $55.4^\circ$ ,  $59.1^\circ$ , and  $65.0^\circ$ , which correspond to (220), (311), (422), (511) and (440) diffraction planes of cubic phase of  $NiCo_2O_4$  (20-0781), respectively. Moreover, all products are of high crystallinity with no impurities. The XRD pattern for the sample  $SS_0$  powders scraped from Ni foam is also obtained, as shown in Fig. S1. One can note that it matches well the elemental contents of sample  $SS_0$  grown on Ni foam, which confirms the chemical formula of sample  $SS_0$  as  $NiCo_2S_4$ .

Figure 2 shows SEM and TEM images of the samples  $SS_0$  and  $S_0$ . There form the nearly vertical  $NiCo_2S_4$  nanosheet arrays with a dimension of  $\sim 5 \mu m$ , which are dense yet homogeneous. Interestingly, almost the whole surfaces of the nanosheet arrays are decorated by nanoneedles (Fig. 2c). From Fig. 2d, one can notice that these  $NiCo_2S_4$  nanosheet arrays have a height of  $\sim 10 \mu m$ . To probe structures of both  $NiCo_2S_4$  and  $NiCo_2O_4$  nanosheet arrays, we conducted TEM imaging of the nanosheets scraped from the Ni foam, as shown in Fig. 2e and 2h. The selected-area diffraction pattern (SADP) reveals that the nanosheets decorated by nanoneedles with a diameter of  $\sim 20$  nm are of polycrystalline nature. Further energy-dispersive X-ray spectroscopy (EDS) spectrum uncovers that the nanosheets are composed of  $NiCo_2S_4$  and  $NiCo_2O_4$  (Fig. 2f and 2i). Figure 2g shows a HRTEM image of the region marked by red box in Fig. 2f, from which lattice fringes from the nanosheets and nanoneedles correspond to the (400) and (220) crystal planes of the  $NiCo_2S_4$  phase. Similarly, lattice fringes shown in Fig. 2j can be indexed as (220) crystal plane of the  $NiCo_2O_4$  phase. These results are also confirmed by the TEM images and EDS spectrum of an individual  $NiCo_2S_4$  nanoneedle that is detached from the nanosheets (Fig. S2). Further EDS quantitative analysis of an individual  $NiCo_2S_4$  nanoneedle in TEM reveals that elemental molar ratio of Ni/Co/S is 1:1.88:3.72, confirming that the Ni-Co sulfide nanoneedles are chemically composed of  $NiCo_2S_4$ .

To extract surface information, we present the  $N_2$  adsorption-desorption isotherm

and pore size distribution curves of the NiCo<sub>2</sub>S<sub>4</sub> sample SS<sub>0</sub> powders scraped from the substrate in Fig. S3. The surface area of the SS<sub>0</sub> powder is estimated to be 36.08 m<sup>2</sup>g<sup>-1</sup> and the pore range is 7~9 nm, indicating that the sample SS<sub>0</sub> is mesoporous and has a large specific surface area.

### 3.2 Growth mechanism

To gain insight into growth mechanism of the nanoneedles-decorated nanosheets, we fabricated a series of nanostructures by altering the dosage of ammonium fluoride and the reaction time. Figure 3 shows SEM images of the nanostructures synthesized with ammonium fluoride of 6 mmol for various reaction time. The NiCo<sub>2</sub>S<sub>4</sub> nanosheet arrays show kind of pony-size and curly nanosheet arrays (SS<sub>1</sub>) when reaction time is 1 h. When the reaction time is increased to 2 h they are transformed to flat and smooth nanosheet arrays (SS<sub>2</sub>). When the reaction time is 3 h, the nanosheet arrays are grown larger but still thin (SS<sub>3</sub>). However, when the reaction time is 4 h, nanoneedles cover the whole surface of nanosheet arrays (SS<sub>0</sub>). Figure e-h presents the corresponding schematic diagram of the growth process. To gain insight into the formation origin of the nanoneedles after a certain period of time, we prepared a series of nanostructures with different dosage of ammonium fluoride for 4 h. Figure 4 shows SEM images and their corresponding schematic diagrams, which reveal a morphology transformation. The nanoneedles arrays in the sample SS<sub>4</sub> are rather dense with a height of ~6 μm when the ammonium fluoride is not added (Fig. 4a and 4b). The NiCo<sub>2</sub>S<sub>4</sub>-NSNs (SS<sub>0</sub>) is obtained when the concentration of ammonium fluoride is increased to 6 mmol. Interestingly, the nanoneedles in the sample SS<sub>5</sub> are vanished when the concentration of ammonium fluoride is increased to 9 mmol. We also replace the NH<sub>4</sub>Cl with NH<sub>4</sub>F, while retaining all other reaction conditions. From the SEM images (Fig. S4), we find that nanowire arrays grow on the Ni foam directly, which is analogous to the case of the sample SS<sub>4</sub> prepared without NH<sub>4</sub>F.

In light of the observations, ammonium fluoride is believed to play an important role in understanding the growth origin of the nanosheet arrays with self-decorated nanoneedles. The ammonium fluoride can be hydrolyzed to generate hydrofluoric acid

and ammonia in hot water, making the whole system strongly acidic. It is known that nanoneedles are much easier to be etched than nanosheets because they have a larger specific surface area and a smaller dimension, which explains that the existence of the ammonium fluoride can efficiently prevent nanoneedles from forming. However, with the reaction proceeding, the ammonium fluoride is gradually consumed, resulting in the formation of nanoneedles. If the ammonium fluoride is enough for the reaction for a period of time, the growth of nanoneedles is inhibited thoroughly.

### 3.3 Electrochemical property

To test their potential application as supercapacitors, we studied electrochemical performance of the SS<sub>0</sub>, SS<sub>5</sub> and S<sub>0</sub> samples. Figure 5a shows the cyclic voltammetry (CV) curves at a sweep rate of 20 mVs<sup>-1</sup> for the SS<sub>0</sub>, SS<sub>5</sub> and S<sub>0</sub> samples. As expected, the region surrounded by the CV curve for the SS<sub>0</sub> electrode is broader than that for the SS<sub>5</sub> and S<sub>0</sub> electrodes. Figure 5b shows the galvanostatic charge-discharge (GCD) curves at a current density of 15 mAcm<sup>-2</sup> (only discharge curves are shown). It takes ~267.0 s for the SS<sub>0</sub> electrode to complete one discharge process, which is longer than that needed for the SS<sub>5</sub> (221.0 s) and S<sub>0</sub> (197.3 s) electrodes, indicating that the SS<sub>0</sub> electrode shows the best electrochemical performance. This can be explained by the fact that the SS<sub>0</sub> sample has the highest surface region in that surfaces of the NiCo<sub>2</sub>S<sub>4</sub> nanosheet arrays are decorated by a large amount of dense nanoneedles, making the surfaces of nanoneedles easily accessible to the electrolyte. In addition, the observed largest specific capacitance may also arise from the fast electron transfer.

To further study the electrochemical behaviors of the SS<sub>0</sub> electrode, we measured systematically the electrochemical performance. Figure 6a shows the CV curves taken with the potential window ranging from -0.1 to 0.7 V at different scan rate. The shape of the CV curves shows a pair of redox peaks: one appears around 0.1 V and the other appears around 0.5 V, which are apparently distinct from the EDLCs characterized by the nearly rectangular CV curves.<sup>32</sup> This means that the Faradaic redox reactions have an impact on the capacity of the SS<sub>0</sub> electrode. With the increase in the voltage sweep rate, the absolute value of the anodic and cathodic peaks increases clearly, revealing a

relatively low resistance of the electrode and the fast redox reactions at the interface between the electrode and electrolyte.<sup>33</sup> Figure 6b shows GCD curves obtained at a potential window 0~0.45 V at different current densities from 15 to 30 mAcm<sup>-2</sup>. The corresponding discharge time is estimated to be 267.0, 176.4, 133.3, and 104.7 s. The decreasing trend almost matches the drop trend of current density. Evidently, the value of potential window decreases slowly around 0.2 V, conforming to the redox peaks in the CV curves. Figure 6c shows curve chart of specific capacitance (Fg<sup>-1</sup>) and areal capacitance (Fcm<sup>-2</sup>) for the SS<sub>0</sub>, SS<sub>5</sub> and S<sub>0</sub> electrode. The SS<sub>5</sub> electrode has a specific (areal) capacitance of 2273.7, 2123.5, 2054.2, and 1979.4 Fg<sup>-1</sup> (7.37, 6.88, 6.66, and 6.41 Fcm<sup>-2</sup>) at a current density of 15, 20, 25, and 30 mAcm<sup>-2</sup>, respectively, while the S<sub>0</sub> electrode has a specific (areal) capacitance of 2121.5, 1770.6, 1546.6, and 1490.3 Fg<sup>-1</sup> (6.58, 5.49, 4.79, and 4.62 Fcm<sup>-2</sup>) at a current density of 15, 20, 25, and 30 mAcm<sup>-2</sup>, respectively. Evidently, the SS<sub>0</sub> electrode exhibits a rather high specific capacitance of 2617.6 Fg<sup>-1</sup> (areal capacitance of 8.9 Fcm<sup>-2</sup>) at a current density of 15 mAcm<sup>-2</sup> and a specific capacitance of 2051.0 Fg<sup>-1</sup> (6.97 Fcm<sup>-2</sup>) even at a high current density of 30 mAcm<sup>-2</sup>. Such an enhanced electrochemical performance for the SS<sub>0</sub> electrode can be attributed to its unusual 3D nanostructures and the intrinsically good electric conductivity.

To check the cycling stability of SS<sub>0</sub> electrode, we present in Fig. 6d the specific capacitance obtained at a current density of 20 mAcm<sup>-2</sup> after cycling for 5000 times. The specific capacitance is 2304.6 Fg<sup>-1</sup> in the beginning and maintains after cycling for 400 times, yet declines very slowly to 2298.1 Fg<sup>-1</sup>. It still retains 93.2% after 5000 cycles, indicating that it has a good cycling stability. To probe microstructure of the SS<sub>0</sub> after 1000 and 5000 cycles, the SS<sub>0</sub> electrode is washed and dried and the SEM imaging is conducted, as shown in the inset of Fig. 6d. The sample after 1000 cycles almost maintains its original 3D nanostructures, despite a little loss of nanoneedles. On the other hand, the sample after 5000 cycles shows thicker nanosheet arrays and the disappearance of nanoneedles due to the ion exchange and chemical reaction of a long time in the KOH solution. To further evaluate performances of SS<sub>0</sub> electrode, we fitted the electrochemical impedance spectra (EIS) data based on an equivalent circuit

model consisting of the solution resistance  $R_s$ , charge-transfer  $R_{ct}$ , double-layer capacitance  $C_{dl}$ , and Warburg resistance  $W$ . Figure 7 shows the curve and equivalent circuit model. From the EIS data, a small  $R_{ct}$  of 0.45  $\Omega$  is obtained for the SS<sub>0</sub> electrode in the Nyquist plots, indicating that the NiCo<sub>2</sub>S<sub>4</sub> nanosheet arrays with self-decorated nanoneedles exhibit outstanding charge-transfer kinetics and fast electron transport. Moreover, we also show phase degrees as a function of frequency for electrode SS<sub>0</sub> in Fig. S1, based on which we confirm that the phase angle of the electrode SS<sub>0</sub> is  $\sim 27^\circ$ . Since the time constant can represent the time for the voltage of capacitor to decrease to  $1/e \approx 36.8\%$ , we calculate it upon the discharge time, which is 267.0, 176.4, 133.3, and 104.7 s at current densities from 15 to 30 mAcm<sup>-2</sup>. The time constant is calculated to be 168.7, 111.5, 84.2, and 66.2 s.

To evaluate the potential of the SS<sub>0</sub> supercapacitor in energy storage application, we design an all-solid-state symmetric supercapacitor by using nickel foam as current collector, the PVA-LiCl as the separator and electrolyte, and the SS<sub>0</sub> as the electrode. From Fig. S6, one can see that the NiCo<sub>2</sub>S<sub>4</sub> sample SS<sub>0</sub> as a symmetric supercapacitor shows a high specific capacitance of 253.2 Fg<sup>-1</sup> at a current density of 4 Ag<sup>-1</sup> and a high energy density of 35.17 Whkg<sup>-1</sup> at 555.6 Wkg<sup>-1</sup>.

#### 4 Conclusions

We have designed and synthesized NiCo<sub>2</sub>S<sub>4</sub> nanosheet arrays with self-decorated nanoneedles on Ni foams for the high-performance pseudocapacitor applications. We demonstrate that the morphologies of various 3D nanostructures such as nanoneedles arrays, nanosheet arrays, and nanoneedles-decorated nanosheet arrays can be tailored by tuning the amount of ammonium fluoride alone during reaction. The as-prepared NiCo<sub>2</sub>S<sub>4</sub>-NSNs electrode is found to show a high specific capacitance of 2617.6 Fg<sup>-1</sup> at the current density of 15 mAcm<sup>-2</sup> and excellent cycling stability by retaining 93.2% even after 5000 cycles. Further comparison of the SS<sub>0</sub> with the SS<sub>5</sub> and S<sub>0</sub> electrodes reveals that the excellent electrochemical performance of NiCo<sub>2</sub>S<sub>4</sub>-NSNs electrode is attributed to its unusual 3D nanostructures and inherent charge transfer and electron transport property. These findings demonstrate that the NiCo<sub>2</sub>S<sub>4</sub> nanosheet arrays with

self-decorated nanoneedles can act as high-performance electrode materials and hold technological promise for supercapacitors and electro-catalytic devices.

### Acknowledgements

This work was supported by the Scientific Research (B) (grant no. 15H04114), Challenging Exploratory Research (grant no. 15K14117), National Nature Science Foundation of China (grant nos. 11332013, 51202302), JSPS and CAS under Japan-China Scientific Cooperation Program, Shorai Foundation for Science and Technology, the Fundamental Research Funds for Central Universities (grant no. 106112015CDJXY130013), and the Chongqing Graduate Student Scientific Research Innovation Project (grant no. CYS14011).

<sup>¶</sup>These authors contributed equally to this work.

\*Corresponding Authors

Corresponding Address: College of Materials Science and Engineering, Chongqing University, Chongqing 400030, China

E-mails: tmliu@cqu.edu.cn (T.L.); zcwang@wpi-aimr.tohoku.ac.jp (Z.C.W.)

### References

- 1 M. F. El-Kady, V. Strong, S. Dubin and R. B. Kaner, *Science*, 2012, **335**, 1326–1330.
- 2 F. Bonaccorso, L. Colombo, G. H. Yu, M. Stoller, V. Tozzini, A. C. Ferrari, R. S. Ruoff and V. Pellegrini, *Science*, 2015, **347**, 1246501–1246509.
- 3 E. J. W. Crossland, N. Noel, V. Sivaram, T. Leijtens, J. A. Alexander-Webber and H. J. Snaith, *Nature*, 2013, **495**, 215–220.
- 4 M. Huang, Y. X. Zhang, F. Li, Z. C. Wang, Alamusi, N. Hu, X. Y. Wen and Q. Liu, *Sci. Rep.*, 2014, **4**, 4518-4527.
- 5 Y. J. Xia, X. J. Liu, Y. J. Bai, H. P. Li, X. L. Deng, X. D. Niu, X. J. Wu, D. F. Zhou, M. F. Lv and Z. C. Wang, *RSC Adv.*, 2012, **2**, 3828-3834.
- 6 M. Acerce, D. Voiry and M. Chhowalla, *Nat. Nanotech.*, 2015, **10**, 313–318.
- 7 L. Shen, L. Yu, H. B. Wu, X. Y. Yu, X. G. Zhang and X. W. Lou, *Nat. Commun.*,

- 2015, **6**, 6694–6701.
- 8 J. T. Mefford, W. G. Hardin, S. Dai, K. P. Johnston and K. J. Stevenson, *Nat. Mater.*, 2014, **13**, 726–732.
- 9 S. J. Peng, L. L. Li, C. C. Li, H. T. Tan, R. Cai, H. Yu, S. Mhaisalkar, M. Srinivasan, S. Ramakrishna and Q. Y. Yan, *Chem. Commun.*, 2013, **49**, 10178–10180.
- 10 Y. Y. Hu, Z. G. Liu, K. W. Nam, O. J. Borkiewicz, J. Cheng, X. Hua, M. T. Dunstan, X. Q. Yu, K. M. Wiaderek, L. S. Du, K. W. Chapman, P. J. Chupas, X. Q. Yang and C. P. Grey, *Nat. Mater.*, 2013, **12**, 1130–1136.
- 11 Z. Y. Zhang, F. Xiao, L. H. Qian, J. W. Xiao, S. Wang and Y. Qi Liu, *Adv. Energy Mater.*, 2014, **4**, 1400064–1400072.
- 12 G. G. Zhang, W. F. Li, K. Y. Xie, F. Yu and H. T. Huang, *Adv. Funct. Mater.*, 2013, **23**, 3675–3681.
- 13 C. Z. Yuan, L. Yang, L. R. Hou, L. F. Shen, X. G. Zhang and X. W. Lou, *Energy Environ. Sci.*, 2012, **5**, 7883–7887.
- 14 G. Q. Zhang, H. B. Wu, H. E. Hoster, M. B. Chan-Park and X. W. Lou, *Energy Environ. Sci.*, 2012, **5**, 9453–9456.
- 15 T. Y. Wei, C. H. Chen, H. C. Chien, S. Y. Lu and C. C. Hu, *Adv. Mater.*, 2010, **22**, 347–351.
- 16 B. Cui, H. Lin, J. B. Li, X. Li, J. Yang and J. Tao, *Adv. Funct. Mater.*, 2008, **18**, 1440–1447.
- 17 G. Q. Zhang and X. W. Lou, *Adv. Mater.*, 2013, **25**, 976–979.
- 18 H. L. Wang, Q. M. Gao and L. Jiang, *Small*, 2011, **7**, 2454–2459.
- 19 X. Y. Liu, S. J. Shi, Q. Q. Xiong, L. Li, Y. J. Zhang, H. Tang, C. D. Gu, X. L. Wang and J. P. Tu, *ACS Appl. Mater. Interfaces*, 2013, **5**, 8790–8795.
- 20 J. W. Xiao, L. Wan, S. H. Yang, F. Xiao and S. Wang, *Nano Lett.*, 2014, **14**, 831–838.
- 21 W. Hu, R. Q. Chen, W. Xie, L. L. Zou, N. Qin and D. H. Bao, *ACS Appl. Mater. Interfaces*, 2014, **6**, 19318–19326.
- 22 T. Peng, Z. Y. Qian, J. Wang, D. L. Song, J. Y. Liu, Q. Liu and P. Wang, *J. Mater.*

- Chem. A*, 2014, **2**, 19376–19382.
- 23 H. C. Chen, J. J. Jiang, L. Zhang, D. D. Xia, Y. D. Zhao, D. Q. Guo, T. Qi and H. Z. Wan, *J. Power Sources*, 2014, **254**, 249–257.
- 24 J. Yang, M. Z. Ma, C. C. Sun, Y. F. Zhang, W. Huang and X. C. Dong, *J. Mater. Chem. A*, 2015, **3**, 1258–1264.
- 25 W. Chen, C. Xia and H. N. Alshareef, *ACS Nano*, 2014, **8**, 9531–9541.
- 26 M. Sun, J. J. Tie, G. Cheng, T. Lin, S. M. Peng, F. Z. Deng, F. Ye and L. Yu, *J. Mater. Chem. A*, 2015, **3**, 1730–1736.
- 27 L. F. Shen, J. Wang, G. Y. Xu, H. S. Li, H. Dou and X. G. Zhang, *Adv. Energy Mater.*, 2015, **5**, 1400977–1400983
- 28 Y. J. Chen, B. H. Qu, L. L. Hu, Z. Xu, Q. H. Li and T. H. Wang, *Nanoscale*, 2013, **5**, 9812–9820.
- 29 Z. C. Wang, M. Saito, K. P. McKenna, L. Gu, S. Tsukimoto, A. L. Shluger and Y. Ikuhara, *Nature*, 2011, **479**, 380–383.
- 30 Z. C. Wang, M. Saito, K. P. McKenna and Y. Ikuhara, *Nat. Commun.*, 2014, **5**, 3239–1–7.
- 31 Z. C. Wang, M. Okude, M. Saito, S. Tsukimoto, A. Ohtomo, M. Tsukada, M. Kawasaki and Y. Ikuhara, *Nat. Commun.*, 2010, **1**, 106–1–7.
- 32 H. Chen, L. F. Hu, Y. Yan, R. C. Che, M. Chen and L. M. Wu, *Adv. Energy Mater.*, 2013, **3**, 1636–1646.
- 33 G. P. Wang, L. Zhang and J. J. Zhang, *Chem. Soc. Rev.*, 2012, **41**, 797–828.

Fig. 1 XRD patterns for the (a) SS<sub>0</sub>, (b) SS<sub>5</sub>, and (c) S<sub>0</sub> samples on Ni foam.

Fig. 2 FESEM and TEM images of the (a-g) SS<sub>0</sub> and (h-j) S<sub>0</sub> samples. (a–c) Typical FESEM images of the SS<sub>0</sub> sample with different magnification. (d) The corresponding front view. (e,f,h,i) TEM images. The insets in (e) and (h) show SAED patterns. The insets in (f) and (i) show EDS spectra. (g,j) HRTEM images of an area marked by red box in (f) and (i).

Fig. 3 FESEM images and schematic diagrams of NiCo<sub>2</sub>S<sub>4</sub> samples synthesized with 6 mmol ammonium fluoride for different reaction time: (a) 1h, (b) 2h, (c) 3h, and (d) 4h. (e-h) Corresponding schematic diagrams.

Fig. 4 FESEM images and schematic diagrams of NiCo<sub>2</sub>S<sub>4</sub> samples synthesized with different concentration of ammonium fluoride for 4 h: (a,b) 0 mmol, (c) 6 mmol, and (d) 9 mmol. The sample prepared without ammonium fluoride is observed from two directions. The insets in (c) and (d) give the magnified SEM images. (e-g) The corresponding schematic diagram.

Fig. 5 (a) CV curves for the SS<sub>0</sub>, SS<sub>5</sub>, and S<sub>0</sub> electrodes measured at a scan rate of 20 mVs<sup>-1</sup>. (b) Galvanostatic discharge curves for the SS<sub>0</sub>, SS<sub>5</sub>, and S<sub>0</sub> electrodes tested at a current density of 15 mAcm<sup>-2</sup>.

Fig. 6 (a) CV curves for the SS<sub>0</sub> electrode measured at a scan rate of 10, 20, and 30 mVs<sup>-1</sup>. (b) Galvanostatic discharge curves obtained at various current densities. (c) Specific or areal capacitance as a function of current density for the SS<sub>0</sub>, SS<sub>5</sub>, and S<sub>0</sub> electrodes. (d) Specific capacitance as a function of cycling number for SS<sub>0</sub> electrode. The SEM images of the samples after 1000 and 5000 cycles are also given.

Fig. 7 EIS Nyquist plots of SS<sub>0</sub> electrode. The inset shows equivalent circuit diagram used to analyze the EIS data.

Figure 1

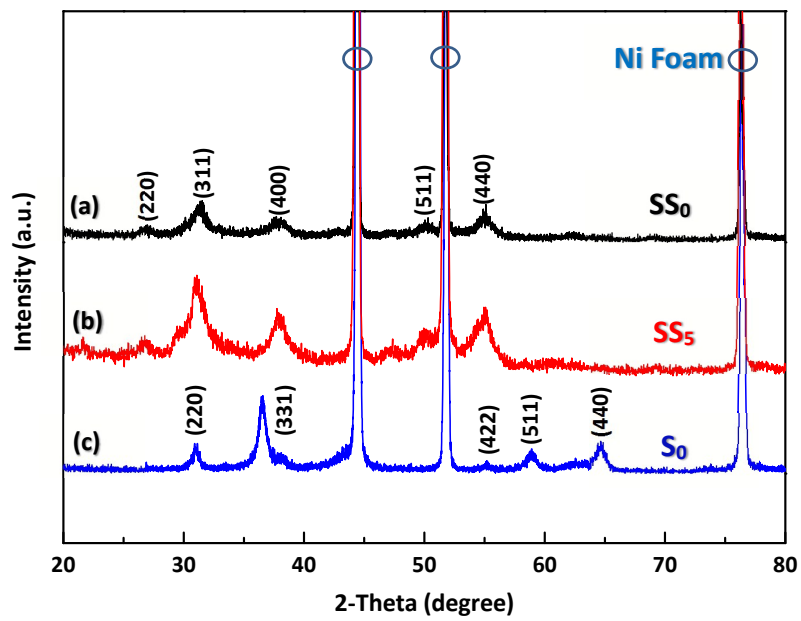


Figure 2

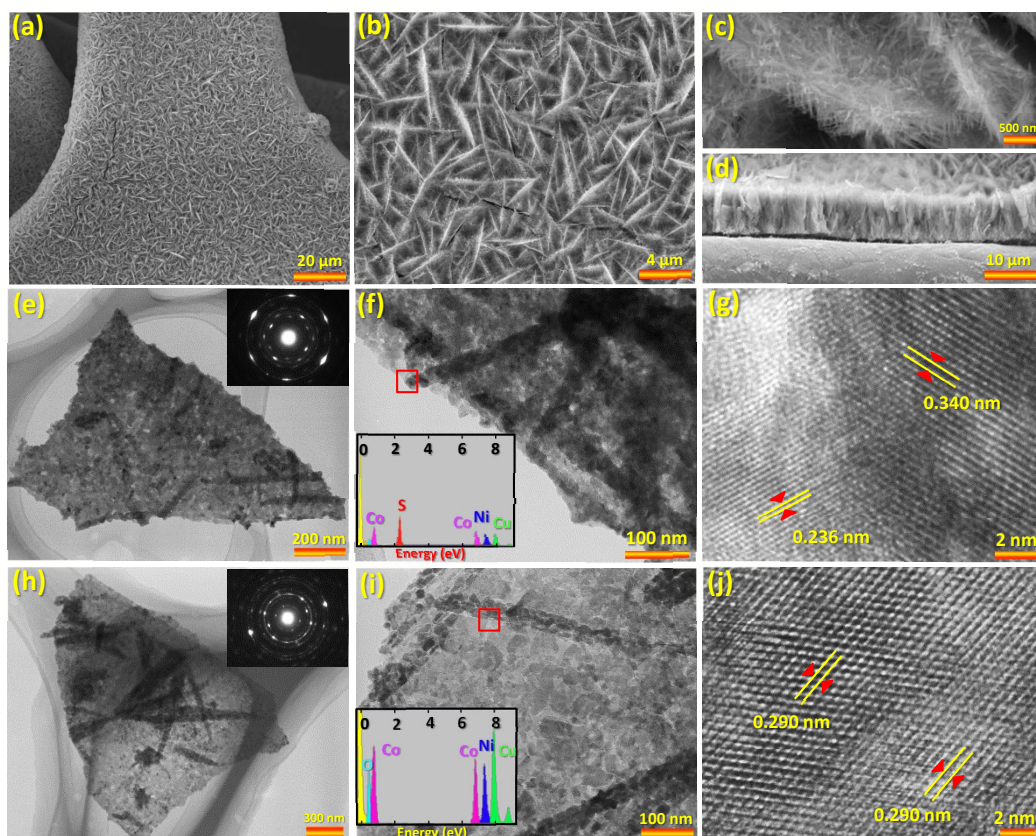


Figure 3

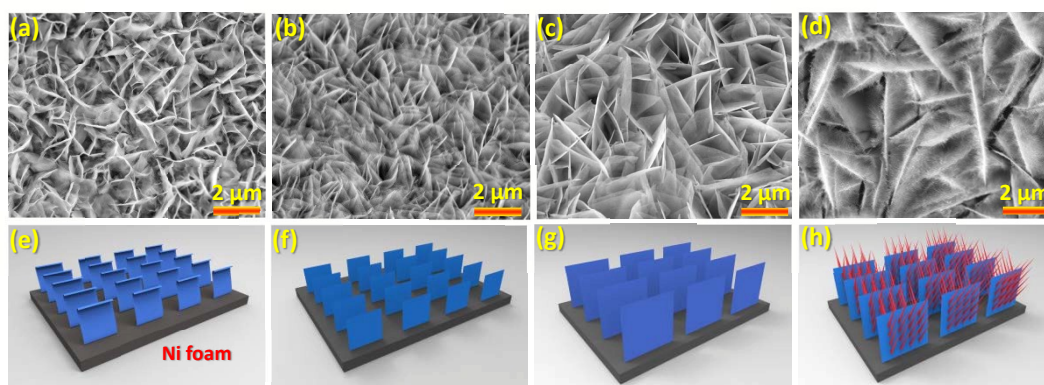


Figure 4

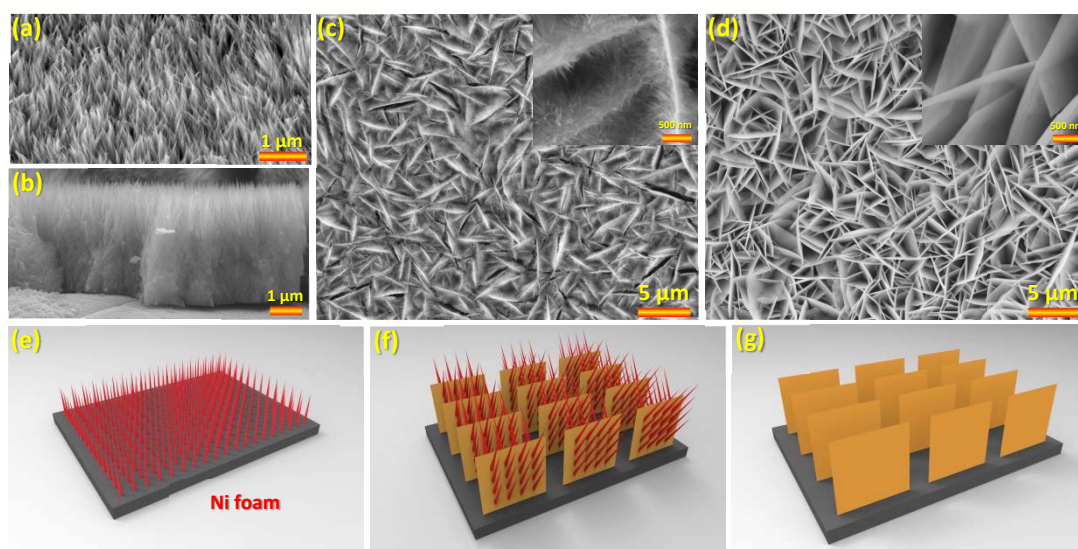


Figure 5

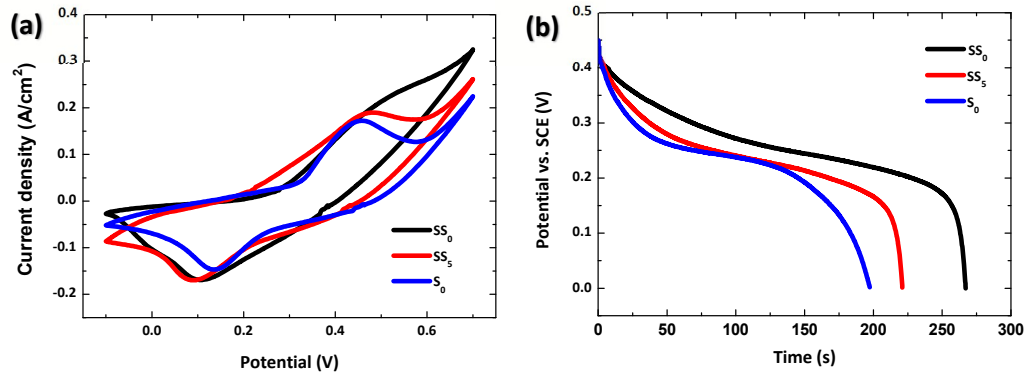


Figure 6

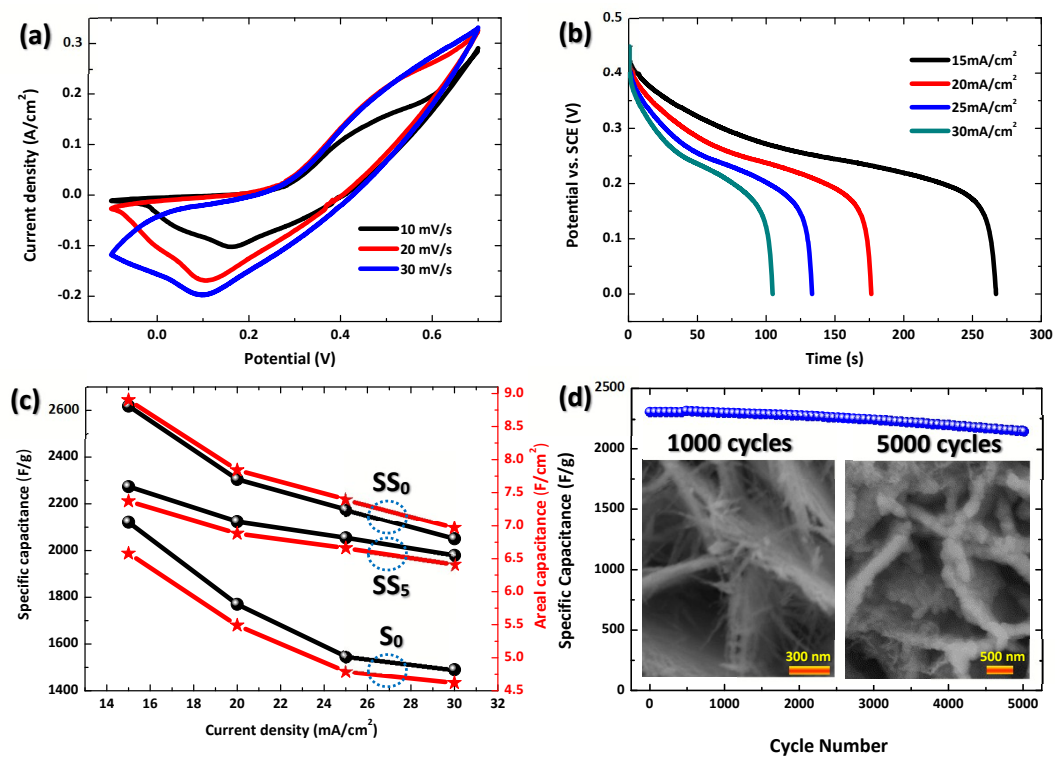


Figure 7

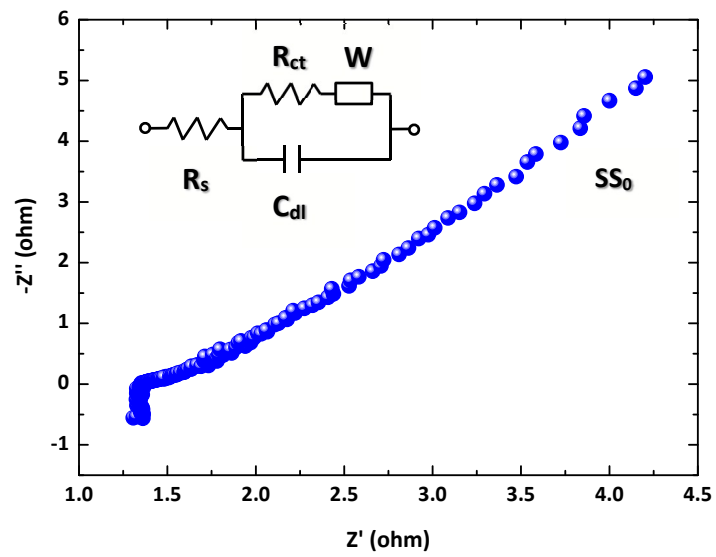


Table of Contents Graphic:

$\text{NiCo}_2\text{S}_4$  nanosheet arrays with self-decorated nanoneedles are synthesized on nickel foams and their electrodes show greatly improved electrochemical performances.

